SUPPLEMENTAL FIGURES

Dev Cell Fig. S1

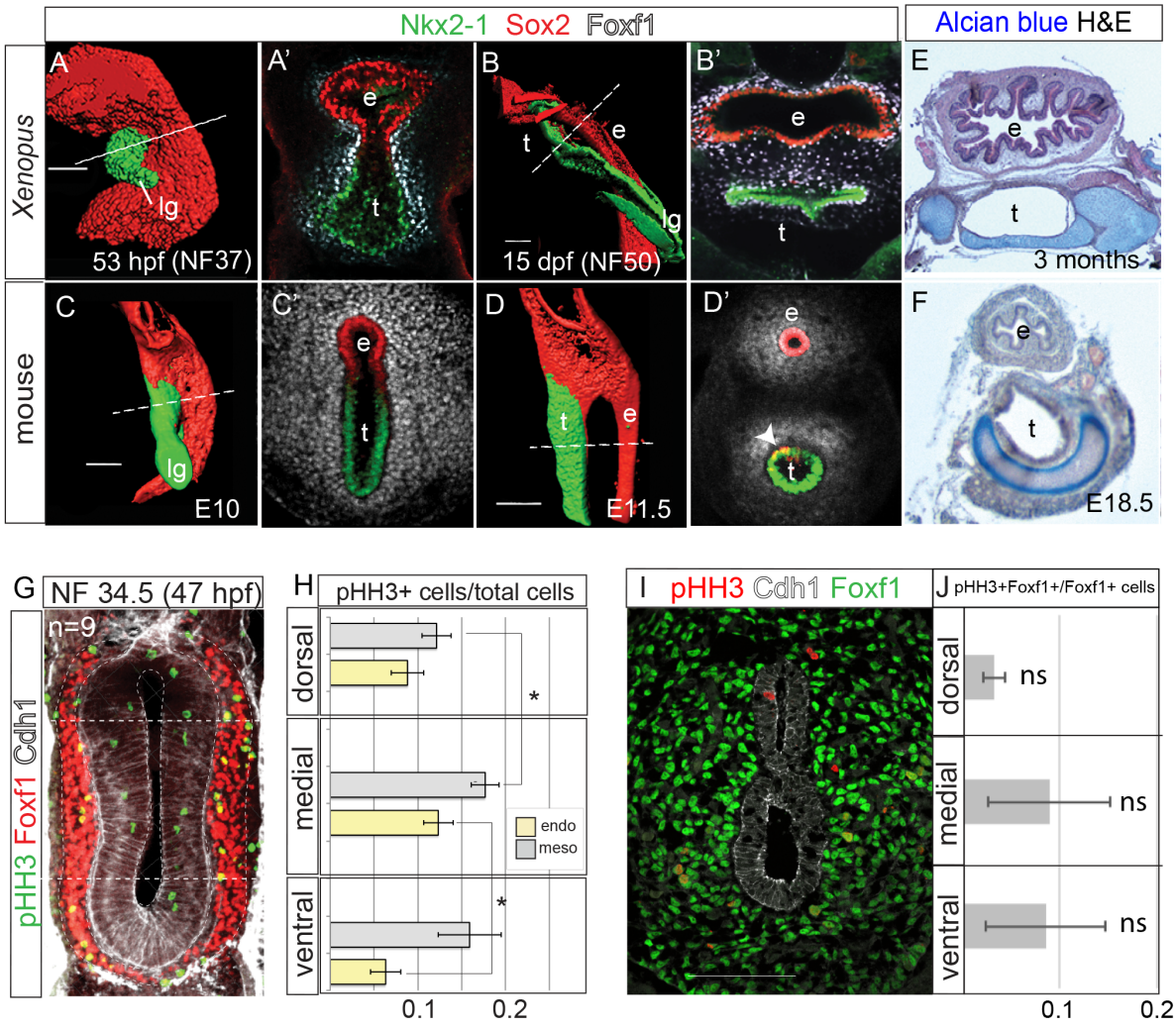

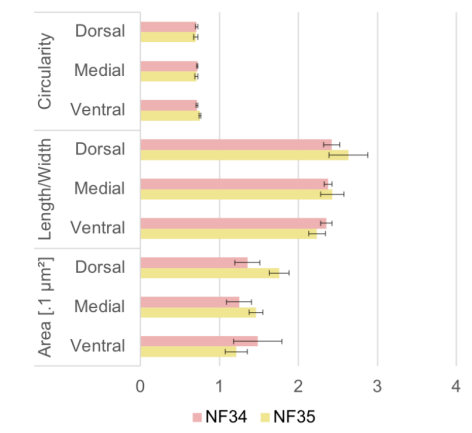

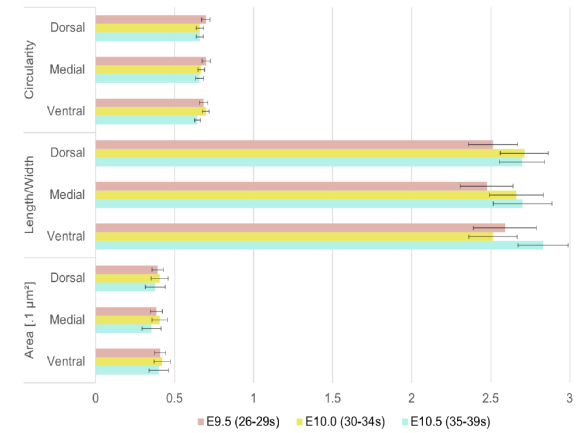

Supplemental Figure S1 (Related to Figure 1) TE Morphogenesis is Conserved in *Xenopus* and Mouse.

S1A-C: Wholemount confocal immunostaining of Sox2, Nkx2-1 and Foxf1 in *X. laevis* (A-B) and mouse (C-D) foregut epithelium. Surface renderings and optical sections show conserved TE morphogenesis, with Sox2+ dorsal foregut giving rise to esophageal epithelium and Nkx2-1+ central foregut giving rise to tracheal and lung epithelium. After separation, rare Sox2+/Nkx2-1+ cells are observed in the ventral esophagus and dorsal trachea (arrowhead in D').

S1E, F: Alcian blue cartilage staining shows similar tracheal differentiation in Xenopus (E) and mouse (F). e = esophagus, t = trachea, lg = laryngeal groove

S1G: Immunostaining of phospho-histone H3-positive (pHH3+) cells, marking proliferating cells in NF34.5 *X. laevis*.

S1H: Quantification of S1G. Endo = (pHH3+Cdh1+)/Cdh1+ cells, meso = (pHH3+Foxf1+)/Foxf1+ cells. The mitotic indices of the medial *X. laevis* endoderm and mesoderm are higher than those seen in the corresponding dorsal and ventral areas. Student's two-tailed t-test, *$p<0.05$.

S1I: Immunostaining of pHH3, Foxf1 and Cdh1 in mouse E10.0 foregut.

S1J: Quantification of S1G, showing no statistically significant difference in pHH3+/Foxf1+ mesoderm cell proliferation from different regions. Two-way ANOVA, *$p<0.05$.

S1K: Size and shape of *Xenopus* mesoderm cells. Average circularity, length/width ratio, and cell area (within .1μm^2) of NF34 and NF35 foregut mesoderm show no statistical difference between regions. Mixed-effects analysis, *$p<0.05$.

S1L: Size and shape of mouse mesoderm cells. Average circularity, length/width ratio, and cell area (within .1μm^2) of E9.5, E10.0 and E10.5 foregut mesoderm show no statistical difference between regions. Mixed-effects analysis, *$p<0.05$.

Dev. Cell Figure S2

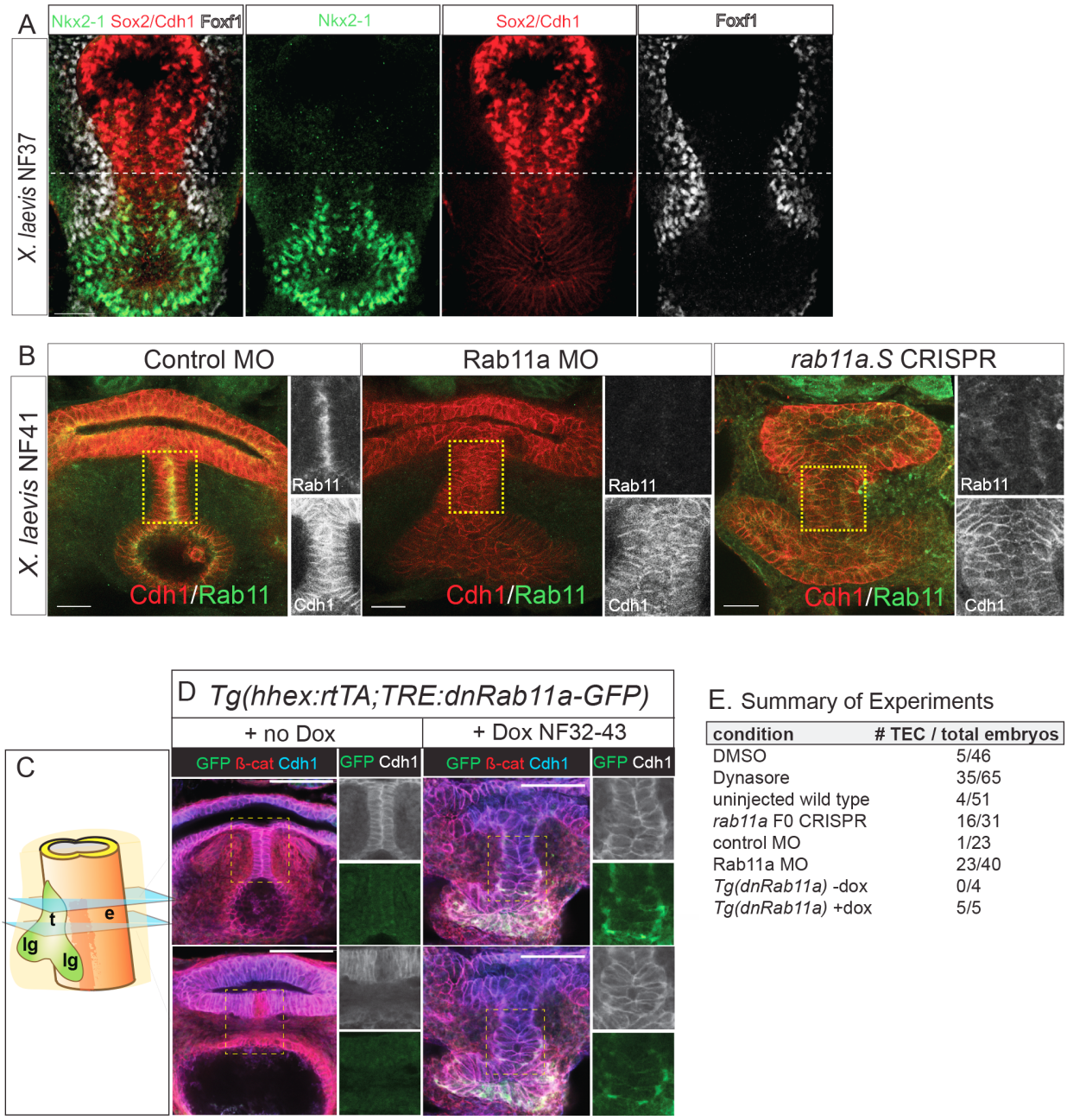

E. Summary of Experiments

condition	# TEC / total embryos
DMSO	5/46
Dynasore	35/65
uninjected wild type	4/51
rab11a F0 CRISPR	16/31
control MO	1/23
Rab11a MO	23/40
Tg(dnRab11a) -dox	0/4
Tg(dnRab11a) +dox	5/5

Supplemental Figure S2 (Related to Figure 2) Rab11a-Dependent Epithelial Remodeling in the Transient Epithelial Septum that Co-Expresses Sox2 and Nkx2-1

S2A: Immunostaining of NF37 *X. laevis* embryos showing co-localization of Sox2 and Nkx2-1 in the transient epithelial septum where the foregut constricts, similar to mouse.

S2B: Immunostaining of Control MO, Rab11 MO and *rab11.S* F0 CRISPR mutant *X. laevis* embryos at NF41 confirming reduced Rab11 protein levels and disorganized epithelium septum relative to control embryos. Scale bar, 50 µm.

S2C: Graphic indicating relative sections of the tracheoesophageal septum and separated trachea and esophagus seen in S2D.

S2D: Sequential optical sections from wholemount immunostaining of transgenic *Tg(hhex:rtTA; TRE:dnRab11a-GFP) X. laevis* embryos at NF42-43. Addition of doxycycline (dox) from NF32-43 resulted in the expression of a dominant-negative Rab11a specifically in the *hhex*+ foregut, which caused disrupted epithelial remodeling similar to Rab11 knockdown. GFP shows dnRab11a protein inappropriately localized to the basal-lateral surface compared to the localization of wildtype Rab11 at the apical surface and fusion point (Fig. 2SD). Scale bar, 100 μm.

S2E: Summary of TEC frequencies in experiments that block Rab11-dependent endosome-mediated epithelial remodeling in *X. laevis* embryos.

Dev Cell Figure S3

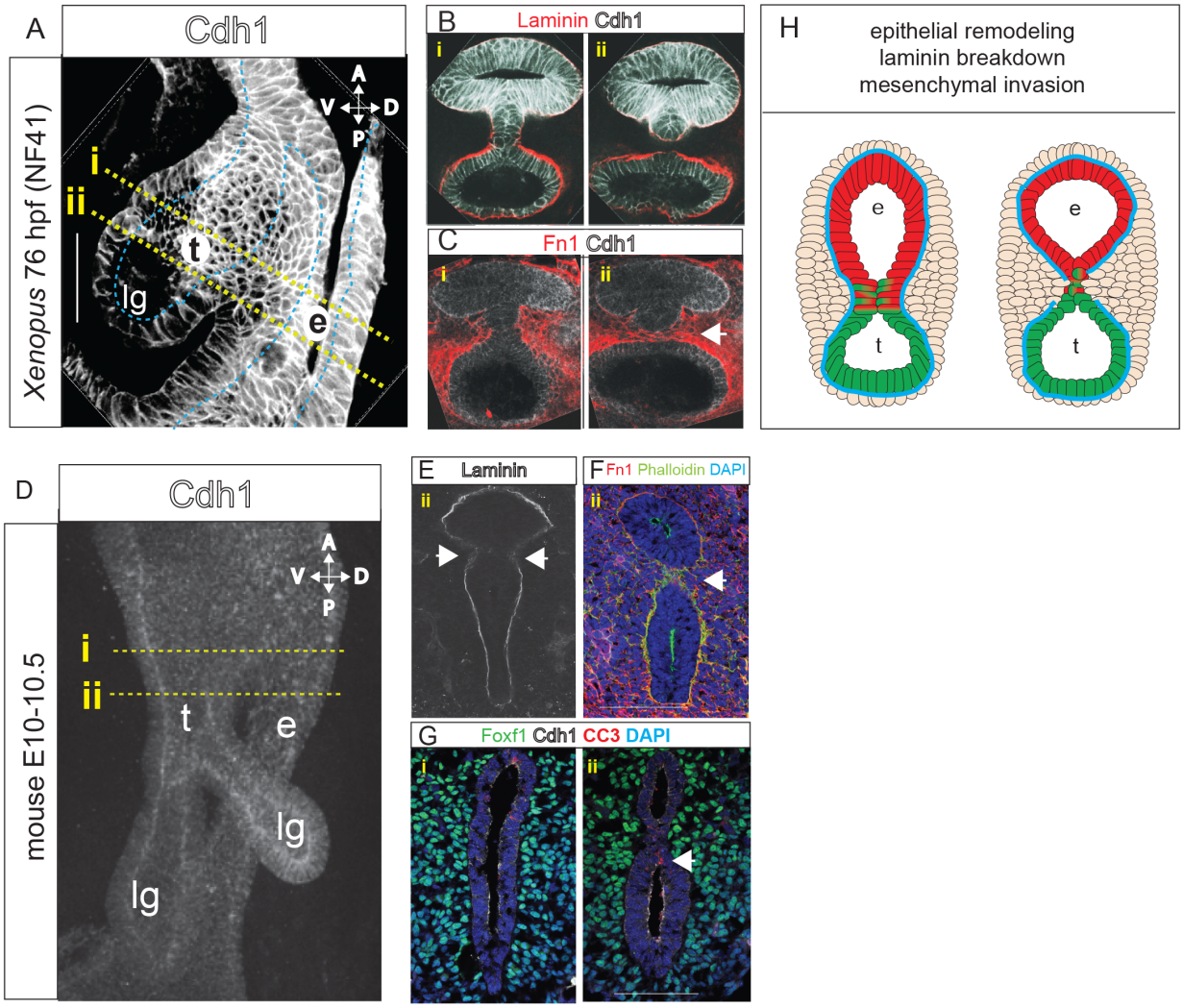

Supplemental Figure S3 (Related to Figure 3) Resolution of the Epithelial Septum
S3A: Wholemount Cdh1 immunostaining of the NF41 *X. laevis* foregut (sagittal view) during (i) and immediately after (ii) TE septum resolution. Trachea (t) and esophagus (e). d; dorsal, v; ventral, a, anterior; p, posterior

S3B: Optical section of Cdh1 and Laminin immunostaining in a NF41 *X. laevis* foregut during (i) and after (ii) TE septum resolution. Laminin decreases around the septum as the epithelial cells downregulate Cdh1 and transition from a columnar to round morphology.

S3C: Optical section of Fibronectin (Fn1) and Cdh1 immunostaining in a NF41 *X. laevis* foregut (i) anterior to and (ii) immediately posterior TE septum resolution. Fn1-enriched mesenchymal cells in the midline between the nascent trachea and esophagus.

S3D: Wholemount Cdh1 immunostaining of an E10.5 mouse embryo showing the constriction of the foregut prior to TE separation.

S3E: Immunostaining showing localized extracellular matrix degradation at the septation point (arrows) in an E11.0 mouse embryo.

S3F: Immunostaining showing enrichment (arrow) of phalloidin and fibronectin just after TE separation in an E11.0 mouse embryo, suggesting medial mesenchymal cell movement. Scale bar, 100 μm.

S3G: Cleaved caspase 3 (CC3)-positive cells, indicating apoptosis before (i) and during (ii) TE separation in an E10.5 mouse embryo. Presence of CC3+ cells in the endoderm during TE septum formation suggests that apoptosis may contribute to TE separation. Arrow denotes CC3 staining in the TE septum. Scale bar, 100 μm.

S3H: Graphical summary of TE septum resolution, including epithelial remodeling at the midline fusion point, bilateral Laminin breakdown on either side of the septum, and mesenchymal invasion as the distinct trachea and esophagus form.

Dev Cell Figure S4

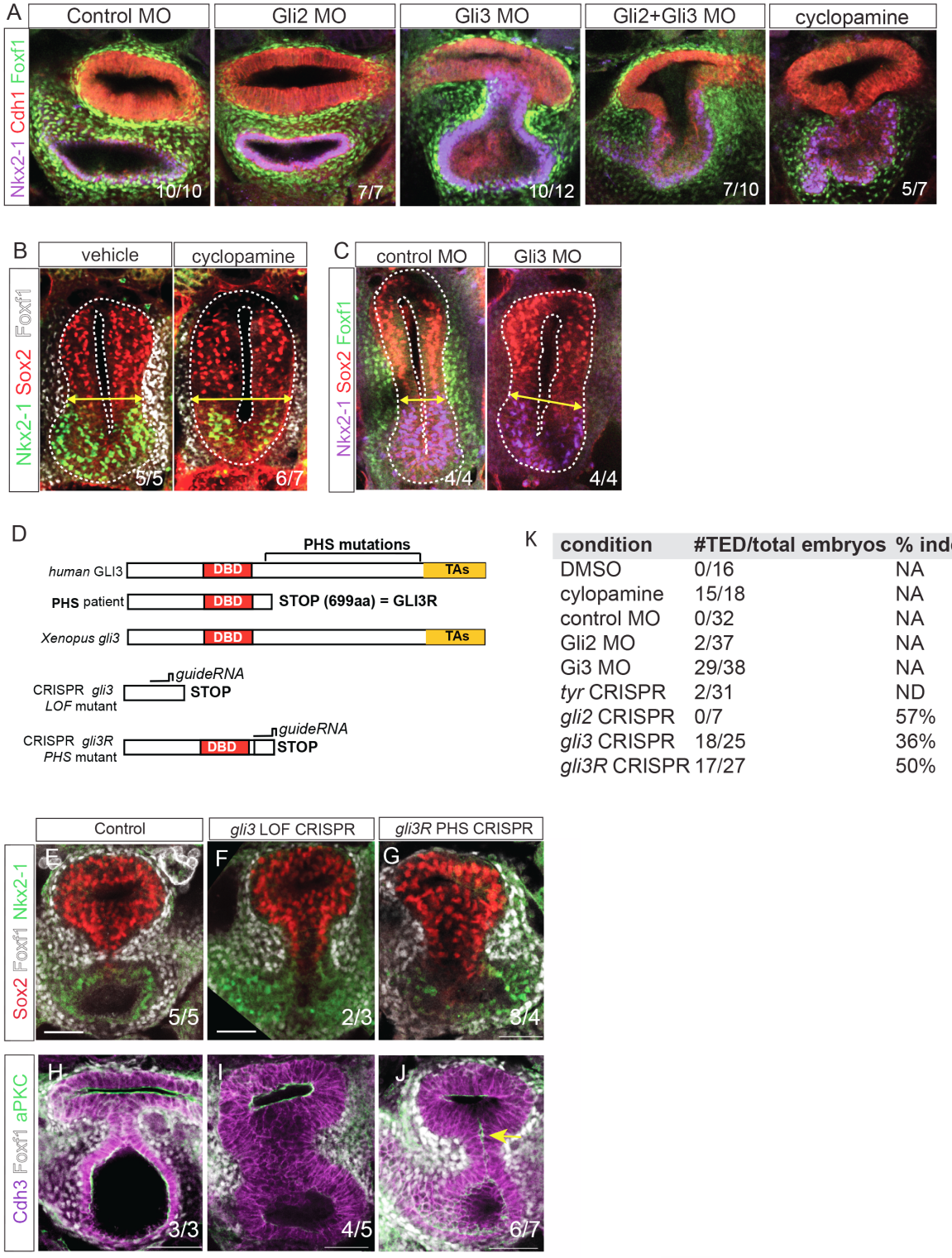

K

condition	#TED/total embryos	% indel
DMSO	0/16	NA
cyclopamine	15/18	NA
control MO	0/32	NA
Gli2 MO	2/37	NA
Gi3 MO	29/38	NA
tyr CRISPR	2/31	ND
gli2 CRISPR	0/7	57%
gli3 CRISPR	18/25	36%
gli3R CRISPR	17/27	50%

Supplemental Figure S4 (Related to Figure 4) HH Signaling and Gli3 are Required for TE Morphogenesis in *Xenopus*

S4A: Immunostaining of Nkx2-1, Cdh1 and Foxf1 in NF42 *X. laevis* embryos injected with previously validated control MOs, Gli2 MOs *or* Gli3 MOs (5-7 ng) (Rankin et al 2016) or treated with the HH antagonist cyclopamine. Gli2 MO embryos show no defect, while Gli3 MO and Gli2+Gli3 MO fail to septate and exhibit a TE cleft. This suggests that *gli3* plays a more critical role than *gli2* during *X. laevis* TE separation. Note higher doses of Gli2+Gli3 MO (10 ng each) fail to pattern the foregut and induce Nkx2-1 as previously shown (Rankin et al 2016).

S4B: Immunostaining of Nkx2-1, Sox2 and Foxf1 in NF35 *X. laevis* embryos treated with cyclopamine exhibit delayed medial constriction as indicated by the yellow arrows and reduced Foxf1+ mesenchyme, but preserve dorsal-ventral patterning, similar to *Shh-/-* mutant mice (Figure 4).

S4C: Immunostaining of Nkx2-1, Sox2 and Foxf1 in NF35 *X. laevis* embryos injected with control MOs or Gli3 MOs, showing delayed medial constriction in Gli3 morphants.

S4D: Schematic of human and *Xenopus* Gli3 proteins and the truncating mutation that results in Pallister Hall Syndrome (PHS). Summary of targeting strategy for CRISPR/Cas9-mediated indel mutagenesis of *X. tropicalis gli3* in embryos. Mutation of *gli3* exon 2 is predicted to result in loss of function (LOF) mutants whereas *gli3R* PHS mutants are predicted to result in a constitutive Gli3 transcriptional repressor.

S4E-G. Immunostaining of Sox2, Foxf1 and Nkx2-1 in control (E) and CRISPR-mediated F0 mutant *X. tropicalis* embryos at NF41. *gli3* LOF mutants (F) and *gli3R* mutants (G) fail to septate and exhibit a persistent TEC, similar to Gli3 MO *X. laevis* embryos.

S4H-J: Immunostaining of Cdh3, Foxf1 and aPKC in control (H) and CRISPR-mediated F0 mutant *X. tropicalis* embryos at NF41. *gli3* LOF mutants (I) show an abnormally thick TE septum that fails to resolve, whereas *gli3R* PHS mutants show persistent aPKC in the septum (arrow), similar to the *Foxg1Cre;Gli3T* mouse mutants, indicating that excessive Gli3R activity prevents remodeling of apical-basal epithelium polarity in the septum and prevents septation.

S4K: Summary of the TED phenotypes in *Xenopus* embryos with disrupted HH/Gli3 activity. The average percentage of damaging indel mutations in CRISPR-mediated F0 mutants from sequencing-TIDE genotyping is shown.